Petroleum Science 22 (2025) 5034–5046

Contents lists available at ScienceDirect

Petroleum Science

journal homepage: www.keaipublishing.com/en/journals/petroleum-science

Original Paper

Fast algorithm of borehole correction library construction for multi-component array induction tool in deviated boreholes

Ya-Zhou Wang [a], Hong-Nian Wang [a,*], Lei Yu [b,**], Yan Bai [c], Shou-Wen Yang [a]

[a] *College of Physics, Jilin University, Changchun, 130012, Jilin, China*
[b] *College of Geo-Exploration Science and Technology, Jilin University, Changchun, 130026, Jilin, China*
[c] *China Petroleum Logging Company, Ltd., Xi'an, 710007, Shaanxi, China*

A R T I C L E I N F O

Article history:
Received 4 July 2025
Received in revised form
7 August 2025
Accepted 24 October 2025
Available online 28 October 2025

Edited by Meng-Jiao Zhou

Keywords:
Multi-component array induction logging
Borehole correction library
3D finite volume method
Contraction high-order Born approximation

A B S T R A C T

The construction of a borehole correction library for the multi-component array induction tool in deviated boreholes involves extensive 3D forward modeling and typically requires significant computational resources. To address this challenge, this paper proposes an efficient algorithm for the library construction based on the 3D finite volume method (FVM) and contraction high-order Born approximation (CHBA). First, the electromagnetic (EM) field solution region is divided into two symmetric subregions based on the symmetry of the correction library model and the EM field. Numerical solution on a single subregion, combined with the symmetry boundary extension technique, enhances the efficiency of the 3D numerical simulation. Second, three reference mud conductivities are selected based on the mud conductivity range, and the CHBA is applied to calculate the EM responses at all mud conductivity nodes rapidly. Third, the number of forward simulation operations is further reduced by exploiting the principle that models with different frequencies and different formation conductivities have equivalent EM responses. Numerical experiments demonstrate the correctness and feasibility of the proposed algorithm. Compared to conventional 3D modeling, the proposed algorithm achieves approximately a 20-fold speedup in library construction, effectively reducing computational resources and time consumption.

1. Introduction

The multi-component induction logging technique utilizes array triaxial transceiver modules (Hussain et al., 2005; Davydycheva et al., 2009; Hou et al., 2013a; Zhu et al., 2017) to simultaneously provide multi-spacing and multi-frequency magnetic field tensors. Consequently, it acquires much richer formation information and has become an important tool for evaluating complex reservoirs, such as anisotropy and thin interaction layers. However, borehole environmental factors such as borehole inclination, borehole radius, mud conductivity, and tool eccentric distance often significantly affect the multi-component induction logging response (Wang et al., 2013; Zhao et al., 2025), resulting in a complex relationship between logging data and true formation parameters. Due to the 3D (Wang et al., 2024a, 2025b) and 2D (Wu et al., 2020, 2023; Yan et al., 2022) numerical simulation and inversion algorithms for electromagnetic (EM) field are often relatively inefficient and have higher requirements for computational conditions (such as large memory and high-speed CPU), methods based on 1D models to process and interpret induction logging data remain the mainstream choice (Deng et al., 2021; Wang et al., 2021, 2023a, 2024c; Yu et al., 2024). Therefore, how to eliminate the effects of the borehole environment has become a key task in multi-component induction logging data processing (Hou et al., 2013b; Bai et al., 2018).

The construction of the borehole correction library is a critical link in borehole environment correction. For the multi-component array induction tool developed by China Petroleum Logging Company, Ltd., Zhu et al. built a borehole correction library using the numerical mode matching (NMM) method in a vertical borehole within anisotropic formation (Zhu et al., 2017), providing a

* Corresponding author.
** Corresponding author.
E-mail addresses: wanghn@jlu.edu.cn (H.-N. Wang), yulei@jlu.edu.cn (L. Yu).
Peer review under the responsibility of China University of Petroleum (Beijing).

https://doi.org/10.1016/j.petsci.2025.10.022
1995-8226/

foundational library for subsequent correction workflows (Bai et al., 2018). Recently, China Petroleum Logging Company, Ltd. needed to build a borehole correction library in deviated boreholes, which involves extensive 3D forward modeling (Hou et al., 2010). Suppose the borehole correction library encompasses 3 frequencies, 1 triaxial transmitter, 15 borehole dip angles, 9 borehole radii, 17 tool eccentric distances, 24 borehole mud conductivities, 24 formation horizontal conductivities, and 15 formation anisotropy coefficients, a total of 178459200 ($3 \times 3 \times 15 \times 9 \times 17 \times 24 \times 24 \times 15$) 3D simulations will be required. If the direct solver is employed, the logging responses of triaxial source and multiple tool eccentric distances can be determined simultaneously, thereby effectively reducing the number of forward simulations. However, the construction of a borehole correction library still requires 3499200 ($3 \times 15 \times 9 \times 24 \times 24 \times 15$) 3D simulations. Assuming 5 min per 3D forward modeling, it requires approximately 33 years of CPU time. While optimizing the number of nodes or using more computational resources could significantly reduce the computational time, improving the algorithm is also essential to enhance the efficiency of library construction. In terms of improving the efficiency of the algorithm, the available approaches include choosing an efficient modeling scheme (Wang et al., 2025b), utilizing the symmetry (Wang et al., 2024b; Li et al., 2025), and using approximation methods (Chen et al., 2021; Wang et al., 2023b, 2025a, 2025c), etc.

There are various options for 3D forward modeling of multi-component array induction tool, such as 3D finite difference method (FDM) (Davydycheva et al., 2009; Sun and Hu, 2022), 3D finite element method (FEM) (Yuan et al., 2020; Wu et al., 2022), 3D finite volume method (FVM) (Haber, 2000; Yu et al., 2022), integral equation method (IEM) (Avdeev et al., 2002; Saputera et al., 2024), etc. Based on our previous research foundation, this study adopts the field-based secondary-field FVM (Wang et al., 2025b) for the 3D forward modeling of the tool. To accelerate the construction of the borehole correction library, three strategies are proposed:

1) Reducing the computational domain by electric field symmetry: In the library, the models and the corresponding EM fields exhibit symmetry in the $y = 0$ plane. By restricting the computational domain to half space using symmetry, the number of grids can be halved, effectively improving the efficiency of the 3D FVM modeling (Wang et al., 2024b; Li et al., 2025).
2) Contraction high-order Born approximation (CHBA) for multi-model modeling: In the library, key parameters (e.g., formation conductivity, borehole mud conductivity, and borehole radius) vary continuously within predefined ranges. Therefore, the construction of the borehole correction library is typically a multi-model problem. This enables us to apply an approximation to significantly enhance the efficiency (Wang et al., 2023b, 2025c).
3) Equivalent calculations in multi-frequency and multi-conductivity simulations: The frequency and conductivity have similar positions in the Helmholtz equation for the electric field in the induction logging. Thus, the multi-frequency and multi-conductivity forward modeling in the construction of the borehole correction library involves some equivalent responses, which help to further reduce the computational workload.

In this paper, we first present the parameters of the borehole correction library and the basic 3D forward modeling approach. We then discuss the electric field symmetry, CHBA, and equivalent calculations in the borehole correction library. Finally, we validate the correctness and feasibility of the proposed algorithm through numerical experiments and discuss the efficiency improvement in library construction.

2. Theory

2.1. Model in borehole correction library

Fig. 1(a) illustrates the basic components of the multi-component induction tool, namely the triaxial co-located transmitter and the triaxial co-located receiver. When building the library, the fine structural details of the tool are ignored. Consequently, the triaxial co-located transmitter is simplified to three orthogonal co-located magnetic dipole point sources, and the three-component magnetic field at the receiver position is computed. Fig. 1(b) presents the model in the borehole correction library, which consists of a deviated borehole and a uniform transversely isotropic (TI) formation, where $x'y'z'$ represents the formation system and xyz represents the borehole system. The implications for the model and tool parameters are provided in Table 1.

The borehole correction library is defined by the eight parameters listed in Table 1. Among these, the transmitter-receiver spacing L and the operating frequency f are determined by the specific tool configuration, while the model parameters should be sampled at enough nodes within predefined ranges as specified in Table 2. Special cases where $\theta = 0$ (vertical well) and $\lambda = 1$ (isotropic formation) can be solved analytically or through NMM. Assuming a tool radius of 0.04 m, the maximum tool eccentric

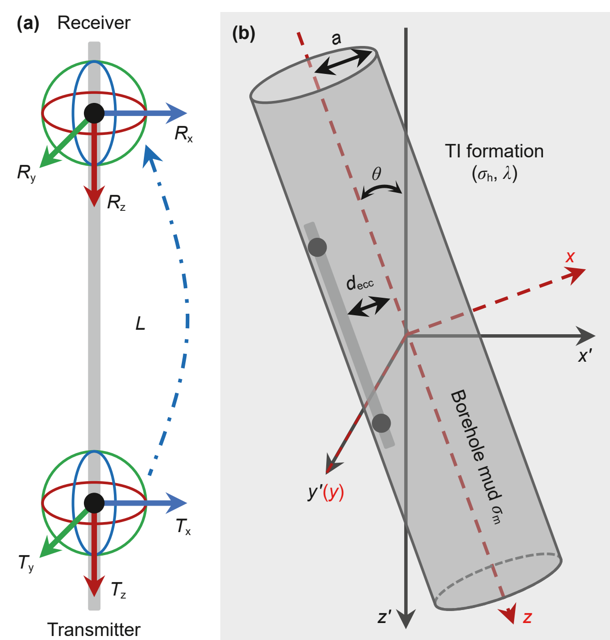

Fig. 1. Schematic diagram of the model in the borehole correction library. **(a)** The basic components of the multi-component induction tool; **(b)** 3D model.

Table 1
Model parameters.

Parameter	Meaning
θ	Borehole dip angle
a	Borehole radius
d_{ecc}	Tool eccentric distance
σ_m	Borehole mud conductivity
σ_h	Horizontal conductivity of TI formation
λ	Anisotropy coefficient of TI formation
L	Transmitter-receiver spacing
f	Transmitter operating frequency

Table 2
Model parameter nodes.

Parameter	Interval	Number	Nodes
θ, °	(0, 90]	15	Select at an interval of 6
a, m	[0.06, 0.22]	9	Select at an interval of 0.02
d_{ecc}, m	[0, a−0.04]	17	Select at an interval of (a−0.04)/16
σ_m, S/m	[0.001, 10]	24	0.001, 0.01, 0.02, 0.04, 0.08, 0.1, 0.2, 0.3, 0.4, 0.5, 0.6, 0.7, 0.8, 0.9, 1, 2, 3, 4, 5, 6, 7, 8, 9, 10
σ_h, S/m	[0.001, 10]	24	0.001, 0.01, 0.02, 0.04, 0.08, 0.1, 0.2, 0.3, 0.4, 0.5, 0.6, 0.7, 0.8, 0.9, 1, 2, 3, 4, 5, 6, 7, 8, 9, 10
λ	(1, 4]	15	Select at an interval of 0.2

distance would be (a−0.04) m. Based on the sampling intervals in Table 2, the library contains a total of 15 × 9 × 17 × 24 × 24 × 15 = 19828800 3D forward models, requiring an immense computational workload. Therefore, optimizing the efficiency of 3D forward modeling is critical for building such a library.

2.2. Field-based secondary-field FVM

The response of the induction tool in the 3D formation model can be obtained by solving the following field-based total-field Helmholtz equation ($e^{-i\omega t}$ is assumed):

$$\nabla\times\nabla\times\mathbf{E}(\mathbf{r},\mathbf{r}_T)-i\omega\mu_0\overline{\boldsymbol{\sigma}}^*(\mathbf{r})\cdot\mathbf{E}(\mathbf{r},\mathbf{r}_T)=i\omega\mu_0\nabla\times\mathbf{M}\delta(\mathbf{r}-\mathbf{r}_T), \tag{1}$$

where $\mathbf{r}_T$ and $\mathbf{r}$ are the positions of the magnetic dipole source and the field point, respectively, $\mathbf{M}$ is a unit magnetic dipole point source in any direction, $\mathbf{E}(\mathbf{r}, \mathbf{r}_T)$ represents the total electric field, $\overline{\boldsymbol{\sigma}}^*(\mathbf{r})=\overline{\boldsymbol{\sigma}}(\mathbf{r})–i\omega\varepsilon_0\bar{\mathbf{I}}$ is the complex conductivity of the model, $\overline{\boldsymbol{\sigma}}(\mathbf{r})$ is the conductivity of the model, $\bar{\mathbf{I}}$ is a unit 3 × 3 tensor, ε_0 is vacuum permittivity, μ_0 is vacuum permeability, i is an imaginary unit, and $\omega=2\pi f$ is the angular frequency.

In 3D FVM modeling, we solve the field-based secondary-field Helmholtz equation instead of directly solving Eq. (1) (Wang et al., 2025b):

$$\nabla\times\nabla\times\mathbf{E}_s(\mathbf{r},\mathbf{r}_T)-i\omega\mu_0\overline{\boldsymbol{\sigma}}^*(\mathbf{r})\cdot\mathbf{E}_s(\mathbf{r},\mathbf{r}_T)=i\omega\mu_0\Delta\mathbf{J}_s(\mathbf{r},\mathbf{r}_T), \tag{2}$$

where $\mathbf{E}_b(\mathbf{r}, \mathbf{r}_T)$ represents the background electric field in the background model, $\mathbf{E}_s(\mathbf{r}, \mathbf{r}_T)=\mathbf{E}(\mathbf{r}, \mathbf{r}_T)-\mathbf{E}_b(\mathbf{r}, \mathbf{r}_T)$ represents the secondary electric field, $\Delta\mathbf{J}_s(\mathbf{r}, \mathbf{r}_T)=\left[\overline{\boldsymbol{\sigma}}^*(\mathbf{r})-\overline{\boldsymbol{\sigma}}_b^*(\mathbf{r})\right]\cdot\mathbf{E}_b(\mathbf{r}, \mathbf{r}_T)$ is the scattered current density, $\overline{\boldsymbol{\sigma}}_b^*(\mathbf{r})=\overline{\boldsymbol{\sigma}}_b(\mathbf{r})–i\omega\varepsilon_0\bar{\mathbf{I}}$ is the complex conductivity of the background model, and $\overline{\boldsymbol{\sigma}}_b(\mathbf{r})$ is the conductivity of the background model. In this paper, we select the uniform anisotropic formation as the background model, and then the borehole is treated as a finite-length cylindrical abnormal body in practical simulations. Additionally, the perfect electric conductor (PEC) boundary condition is applied at the outer boundary of the computational domain.

$$\mathbf{n}\times\mathbf{E}_s(\mathbf{r},\mathbf{r}_T)|_{\partial\Omega}=0, \tag{3}$$

where $\partial\Omega$ represents the outer boundary of the computational domain and $\mathbf{n}$ represents the outer normal vector of the boundary.

Let N_x, N_y, and N_z denote the number of grids in the x, y, and z directions, respectively. Then, using the FVM to discretize Eq. (2) will generate $M=(N_x+1)\times N_y\times N_z+N_x\times(N_y+1)\times N_z+N_x\times N_y\times(N_z+1)$ unknowns, and eventually obtain an M-dimensional algebraic equation:

$$\overline{\mathbf{F}}\mathbf{u}(\mathbf{r}_T)=\mathbf{b}(\mathbf{r}_T), \tag{4}$$

where the coefficient matrix $\overline{\mathbf{F}}$ is a known $M\times M$ asymmetric sparse complex matrix, $\mathbf{u}(\mathbf{r}_T)$ is the M-dimensional unknown column vector about the discrete secondary electric field, $\mathbf{b}(\mathbf{r}_T)$ is the discrete result of the right-hand side of Eq. (2).

Considering that the triaxial source of the tool and the borehole correction library includes multiple tool eccentric distances d_{ecc}, the right-hand sides generated by N sources are combined to form an $M\times N$ matrix $\overline{\mathbf{B}}=(\mathbf{b}_1, \ldots, \mathbf{b}_N)$. Similarly, the unknown column vector can also form an $M\times N$ matrix $\overline{\mathbf{U}}=(\mathbf{u}_1, \ldots, \mathbf{u}_N)$. Since the coefficient matrix $\overline{\mathbf{F}}$ is kept fixed in each calculation window, the discrete secondary electric field generated by N sources can be solved simultaneously using a direct solver

$$\overline{\mathbf{U}}=\overline{\mathbf{F}}^{-1}\overline{\mathbf{B}}, \tag{5}$$

where the inverse matrix $\overline{\mathbf{F}}^{-1}$ is obtained by the parallel direct sparse solver (PARDISO). By applying linear interpolation, the electric and magnetic fields at any source location and field point can then be determined.

2.3. Reducing the computational domain by electric field symmetry

When building the borehole correction library, the model adopts the $y=0$ plane as the symmetry plane (see Fig. 1(a)). Therefore, the EM field along the $y=0$ plane is symmetric/anti-symmetric. This characteristic enables the computational domain to be halved. The symmetry properties of the electric field are summarized in Table 3, where the symbol "−" represents the domain of $y<0$ and "+" represents the domain of $y>0$.

By setting symmetry boundary extension conditions on the $y=0$ plane based on the symmetry relations provided in Table 3, the electric field values within the domain $y\le 0$ (or $y\ge 0$) can be computed. Note that the electric fields excited by magnetic dipole sources oriented in the x- and z-directions share the same symmetry relations, which differ from those generated by the y-direction magnetic dipole source. Consequently, after discretizing Eq. (2) with the FVM, two algebraic equations are derived in the domain $y\le 0$:

$$\begin{cases}\overline{\mathbf{F}}_{xz}\overline{\mathbf{U}}_{xz}=\overline{\mathbf{B}}_{xz}\\ \overline{\mathbf{F}}_y\overline{\mathbf{U}}_y=\overline{\mathbf{B}}_y\end{cases}, \tag{6}$$

where the coefficient matrix $\overline{\mathbf{F}}_{xz}$, the electric field $\overline{\mathbf{U}}_{xz}$, and the right-hand side $\overline{\mathbf{B}}_{xz}$ correspond to the magnetic dipole sources

Table 3
Symmetry relation of the electric field.

Source direction	$y=0$	$y\neq 0$
x	$E_x=0$, $E_y\neq 0$, $E_z=0$	$E_{x+}=-E_{x-}$, $E_{y+}=E_{y-}$, $E_{z+}=-E_{z-}$
y	$E_x\neq 0$, $E_y=0$, $E_z\neq 0$	$E_{x+}=E_{x-}$, $E_{y+}=-E_{y-}$, $E_{z+}=E_{z-}$
z	$E_x=0$, $E_y\neq 0$, $E_z=0$	$E_{x+}=-E_{x-}$, $E_{y+}=E_{y-}$, $E_{z+}=-E_{z-}$

oriented in the x- and z-directions; $\overline{\mathbf{F}}_y$, $\overline{\mathbf{U}}_y$, and $\overline{\mathbf{B}}_y$ correspond to the magnetic dipole source oriented in the y-direction. The dimensions of both $\overline{\mathbf{F}}_{xz}$ and $\overline{\mathbf{F}}_y$ are $M' = (N_x + 1) \times N_y/2 \times N_z + N_x \times (N_y/2 + 1) \times N_z + N_x \times N_y/2 \times (N_z + 1)$.

Similarly to Eq. (5), we need to perform two direct solution procedures

$$\begin{cases} \overline{\mathbf{U}}_{xz} = \overline{\mathbf{F}}_{xz}^{-1}\overline{\mathbf{B}}_{xz} \\ \overline{\mathbf{U}}_y = \overline{\mathbf{F}}_y^{-1}\overline{\mathbf{B}}_y \end{cases}. \tag{7}$$

Since $M' \approx M/2$, the computational complexity of solving Eq. (7) is lower than that of Eq. (5), thereby significantly enhancing the computational efficiency of 3D forward modeling.

2.4. Contraction high-order Born approximation

Suppose the conductivity distribution of the reference model is $\overline{\boldsymbol{\sigma}}(\mathbf{r})$, where the borehole dip angle θ, the formation horizontal conductivity σ_{h}, the anisotropy coefficient λ, the borehole radius a, and the borehole mud conductivity σ_{m} take specific values. The borehole correction library contains a series of mud conductivities, and we can regard any mud conductivity σ'_{m} as the sum of the mud conductivity σ_{m} in the reference model and the change in mud conductivity $\Delta\sigma_{\mathrm{m}}$, that is, $\sigma'_{\mathrm{m}} = \sigma_{\mathrm{m}} + \Delta\sigma_{\mathrm{m}}$. Then, the change in electric field $\Delta\mathbf{E}(\mathbf{r}, \mathbf{r}_{\mathrm{T}})$ caused by $\Delta\sigma_{\mathrm{m}}$ satisfies the equation

$$\nabla \times \nabla \times \Delta\mathbf{E}(\mathbf{r},\mathbf{r}_{\mathrm{T}}) - i\omega\mu_0\overline{\boldsymbol{\sigma}}^*(\mathbf{r}) \cdot \Delta\mathbf{E}(\mathbf{r},\mathbf{r}_{\mathrm{T}}) = i\omega\mu_0\mathbf{J}^{\mathrm{t}}(\mathbf{r},\mathbf{r}_{\mathrm{T}}), \tag{8}$$

where

$$\mathbf{J}^{\mathrm{t}}(\mathbf{r},\mathbf{r}_{\mathrm{T}}) = \Delta\sigma_{\mathrm{m}}(\mathbf{r})\Delta\mathbf{E}(\mathbf{r},\mathbf{r}_{\mathrm{T}}) + \mathbf{J}(\mathbf{r},\mathbf{r}_{\mathrm{T}}) = \Delta\sigma_{\mathrm{m}}(\mathbf{r})\Delta\mathbf{E}(\mathbf{r},\mathbf{r}_{\mathrm{T}}) + \Delta\sigma_{\mathrm{m}}(\mathbf{r})\mathbf{E}(\mathbf{r},\mathbf{r}_{\mathrm{T}}) \tag{9}$$

is the total scattered current density, $\mathbf{J}(\mathbf{r}, \mathbf{r}_{\mathrm{T}}) = \Delta\sigma_{\mathrm{m}}(\mathbf{r})\mathbf{E}(\mathbf{r}, \mathbf{r}_{\mathrm{T}})$ represents the first-order scattered current density.

Eq. (8) can be quickly solved by approximation. Based on the CHBA (Wang et al., 2025c), a more concise expansion expression of the change in electric field can be further given (see Appendix):

$$\Delta\mathbf{E}(\mathbf{r},\mathbf{r}_{\mathrm{T}}) = \sum_{l=1}^{\infty}\boldsymbol{\lambda}_l(\mathbf{r},\mathbf{r}_{\mathrm{T}}), \tag{10}$$

where the l-order scattered electric field $\boldsymbol{\lambda}_l$ satisfies the equation

$$\nabla \times \nabla \times \boldsymbol{\lambda}_l(\mathbf{r},\mathbf{r}_{\mathrm{T}}) - i\omega\mu_0\overline{\boldsymbol{\sigma}}^*(\mathbf{r}) \cdot \boldsymbol{\lambda}_l(\mathbf{r},\mathbf{r}_{\mathrm{T}}) = \mathbf{b}_l(\mathbf{r},\mathbf{r}_{\mathrm{T}}), \tag{11}$$

in which the right-hand side $\mathbf{b}_l(\mathbf{r}, \mathbf{r}_{\mathrm{T}})$ is

$$\mathbf{b}_l(\mathbf{r},\mathbf{r}_{\mathrm{T}}) = \begin{cases} i\omega\mu_0\dfrac{2\overline{\boldsymbol{\sigma}}(\mathbf{r})}{2\overline{\boldsymbol{\sigma}}(\mathbf{r}) + \Delta\sigma_{\mathrm{m}}(\mathbf{r})\overline{\mathbf{I}}}\cdot\mathbf{J}(\mathbf{r},\mathbf{r}_{\mathrm{T}}), l = 1 \\ R(\mathbf{r})[i\omega\mu_0 2\overline{\boldsymbol{\sigma}}(\mathbf{r})\cdot\boldsymbol{\lambda}_{l-1}(\mathbf{r},\mathbf{r}_{\mathrm{T}}) + \mathbf{b}_{l-1}(\mathbf{r},\mathbf{r}_{\mathrm{T}})], l = 2, 3, \cdots \end{cases} \tag{12}$$

and the contraction factor $R(\mathbf{r})$ is

$$R(\mathbf{r}) = \frac{\Delta\sigma_{\mathrm{m}}(\mathbf{r})}{2\sigma_{\mathrm{m}}(\mathbf{r}) + \Delta\sigma_{\mathrm{m}}(\mathbf{r})}. \tag{13}$$

Due to the physical limitation that the conductivity is greater than 0, the maximum value $R_{\sup} = \sup[R(\mathbf{r})]$ of the contraction factor is always less than 1, and the smaller $R_{\sup}$ is, the faster Eq. (10) converges. After selecting the appropriate truncation order L_{T} (Wang et al., 2025c), Eq. (10) can be truncated to

$$\Delta\mathbf{E}(\mathbf{r},\mathbf{r}_{\mathrm{T}}) \approx \Delta\mathbf{E}^{L_{\mathrm{T}}}(\mathbf{r},\mathbf{r}_{\mathrm{T}}) = \sum_{l=1}^{L_{\mathrm{T}}}\boldsymbol{\lambda}_l(\mathbf{r},\mathbf{r}_{\mathrm{T}}). \tag{14}$$

Ultimately, the total EM field can be expressed as

$$\mathbf{E}'(\mathbf{r},\mathbf{r}_{\mathrm{T}}) \approx \mathbf{E}(\mathbf{r},\mathbf{r}_{\mathrm{T}}) + \Delta\mathbf{E}^{L_{\mathrm{T}}}(\mathbf{r},\mathbf{r}_{\mathrm{T}}), \mathbf{H}'(\mathbf{r},\mathbf{r}_{\mathrm{T}}) \approx \frac{\nabla \times \mathbf{E}'(\mathbf{r},\mathbf{r}_{\mathrm{T}})}{i\omega\mu_0}. \tag{15}$$

Note that Eqs. (2) and (11) are identical except for the right-hand side. Therefore, the solution form of Eq. (11) is the same as that of Eq. (7)

$$\begin{cases} \overline{\mathbf{U}}_{xz,l} = \overline{\mathbf{F}}_{xz}^{-1}\overline{\mathbf{B}}_{xz,l} \\ \overline{\mathbf{U}}_{y,l} = \overline{\mathbf{F}}_y^{-1}\overline{\mathbf{B}}_{y,l} \end{cases}. \tag{16}$$

Since $\overline{\mathbf{F}}_{xz}^{-1}$ and $\overline{\mathbf{F}}_y^{-1}$ can be reused, based on the simulation result when the mud conductivity is σ_{m}, the simulation result of the mud conductivity $\sigma'_{\mathrm{m}} = \sigma_{\mathrm{m}} + \Delta\sigma_{\mathrm{m}}$ can be obtained quickly.

When we consider the mud conductivity only, the changes in conductivity corresponding to different mud conductivities differ by a constant multiple. This feature enables a significant reduction in the computational complexity of the CHBA. For this purpose, consider that the change in the mud conductivity changes from $\Delta\sigma_{\mathrm{m}}$ to $c_\sigma\Delta\sigma_{\mathrm{m}}$, that is, mud conductivity changes from $\sigma'_{\mathrm{m}} = \sigma_{\mathrm{m}} + \Delta\sigma_{\mathrm{m}}$ to $\sigma'_{c,\mathrm{m}} = \sigma_{\mathrm{m}} + c_\sigma\Delta\sigma_{\mathrm{m}}$, where c_σ is a constant. Then, the right-hand side of Eq. (11) becomes

$$\begin{aligned} \mathbf{b}_{c'_\sigma,l}(\mathbf{r},\mathbf{r}_{\mathrm{T}}) &= \left[c_\sigma\frac{2\sigma_{\mathrm{m}}(\mathbf{r}) + \Delta\sigma_{\mathrm{m}}(\mathbf{r})}{2\sigma_{\mathrm{m}}(\mathbf{r}) + c_\sigma\Delta\sigma_{\mathrm{m}}(\mathbf{r})}\right]^l\mathbf{b}_l(\mathbf{r},\mathbf{r}_{\mathrm{T}}) \\ &= {c'_\sigma}^l\mathbf{b}_l(\mathbf{r},\mathbf{r}_{\mathrm{T}}), l = 1, 2, 3, \cdots. \end{aligned} \tag{17}$$

When there are only changes in mud conductivity, $c'_\sigma = c_\sigma\frac{2\sigma_{\mathrm{m}}(\mathbf{r}) + \Delta\sigma_{\mathrm{m}}(\mathbf{r})}{2\sigma_{\mathrm{m}}(\mathbf{r}) + c_\sigma\Delta\sigma_{\mathrm{m}}(\mathbf{r})}$ is a constant. According to Eq. (14), the electric fields in the two models have the following relationship:

$$\Delta\mathbf{E}_{c'_\sigma}(\mathbf{r},\mathbf{r}_{\mathrm{T}}) \approx \Delta\mathbf{E}_{c'_\sigma}^{L_{\mathrm{T}}}(\mathbf{r},\mathbf{r}_{\mathrm{T}}) = \sum_{l=1}^{L_{\mathrm{T}}}{c'_\sigma}^l\boldsymbol{\lambda}_l(\mathbf{r},\mathbf{r}_{\mathrm{T}}). \tag{18}$$

Assuming the change in electric field under the mud conductivity $\sigma'_{\mathrm{m}} = \sigma_{\mathrm{m}} + \Delta\sigma_{\mathrm{m}}$ has been determined via Eq. (14), Eq. (18) (with $|c'_\sigma| \le 1$) establishes an algebraic relationship between the change in electric field and the mud conductivity. This formulation enables rapid computation of electric fields for arbitrarily dense sampling points across the mud conductivity interval.

2.5. Equivalent calculations in multi-frequency and multi-conductivity simulations

The construction of the borehole correction library requires calculations at multiple frequencies (e.g., 26, 52, and 104 kHz) and extensive different model conductivities. Since the permittivity in the induction logging has little influence on the measurement results, there are some equivalent responses in the modeling of multi-frequency and multi-conductivity. To demonstrate this point, consider the frequency f becomes $c_f f$, then Eq. (1) becomes

$$\nabla \times \nabla \times \mathbf{E}(\mathbf{r},\mathbf{r}_{\mathrm{T}}) - ic_f\omega\mu_0\overline{\boldsymbol{\sigma}}^*(\mathbf{r}) \cdot \mathbf{E}(\mathbf{r},\mathbf{r}_{\mathrm{T}}) = ic_f\omega\mu_0\nabla \times \mathbf{M}\delta(\mathbf{r} - \mathbf{r}_{\mathrm{T}}). \tag{19}$$

That is

$$\nabla \times \nabla \times \mathbf{E}(\mathbf{r}, \mathbf{r}_\mathrm{T}) - i\omega\mu_0 c_f \overline{\boldsymbol{\sigma}}^*(\mathbf{r}) \cdot \mathbf{E}(\mathbf{r}, \mathbf{r}_\mathrm{T}) = i\omega\mu_0 \nabla \times c_f \mathbf{M}\delta(\mathbf{r} - \mathbf{r}_\mathrm{T}). \tag{20}$$

Eqs. (19) and (20) indicate that under specific conditions, different conductivities and frequencies have the same magnetic field response. For example, when the borehole dip angle θ, the borehole radius a, and the formation anisotropy coefficient λ remain constant, the following three situations should produce identical magnetic field responses: 1) frequency $f = 26$ kHz, borehole mud conductivity σ_m, formation horizontal conductivity σ_h; 2) frequency $f = 52$ kHz, borehole mud conductivity $\sigma_\mathrm{m}/2$, formation horizontal conductivity $\sigma_\mathrm{h}/2$; 3) frequency $f = 104$ kHz, borehole mud conductivity $\sigma_\mathrm{m}/4$, and formation horizontal conductivity $\sigma_\mathrm{h}/4$. Moreover, we do not impose any restrictions on the conductivity $\overline{\boldsymbol{\sigma}}^*(\mathbf{r})$. These conclusions hold for any model parameters (such as θ, a, λ, d_ecc, etc.). Based on the above features, the computational workload of building the library can be further reduced.

Under the condition of fixed formation conductivity anisotropy coefficient λ, the borehole mud conductivity and the formation horizontal conductivity need to change by the same multiple to satisfy the above conditions. Fortunately, a fast calculation method for the arbitrary borehole mud conductivity is provided in Section 2.4. Therefore, only the formation horizontal conductivity needs to be focused on, and the number of equivalent calculations increases significantly.

3. Numerical experiments

This section validates the proposed algorithm and evaluates its computational efficiency. All simulations assume that the borehole dip angle is 30°, the formation anisotropy coefficient is 2, and the borehole radius is 0.2 m. Here, we choose a relatively large borehole radius (the borehole effect is more pronounced) to more effectively test the accuracy of the algorithm. In Sections 3.1–3.4, the transmitter-receiver spacing L is 1.8 m, the frequencies $f = 26$, 52, and 104 kHz, and the calculation results of the imaginary part of the magnetic field are given. In Section 3.5, the apparent conductivity charts are calculated for the borehole mud conductivity, the formation horizontal conductivity, and the tool eccentric distance based on the physical structure of the tool. The grid numbers in the x-, y-, and z-directions for the complete FVM are $N_x = 52$, $N_y = 52$, and $N_z = 122$, respectively. The calculational domain is set to twice the skin depth, but is limited to a range of 5–50 m. The skin depth is calculated based on the vertical conductivity of the formation. Simulations are performed on a workstation with an Intel(R) Xeon(R) Gold 6338 CPU. The number of threads for all simulations is 10, and the actual operating frequency of the CPU is approximately 4.0 GHz.

3.1. Algorithm verification

To validate the algorithm, the formation horizontal conductivity is fixed at 0.2 S/m, and two tool eccentric distances of 0 and 0.08 m are tested. The magnetic field responses of the tool are simulated under different borehole mud conductivities and compared with the COMSOL solutions. Figs. 2 and 3 show the results for $d_\mathrm{ecc} = 0$ and 0.08 m, respectively. The calculation results include the three principal components (H_{xx}, H_{yy}, H_{zz}) and two cross components (H_{zx}, H_{xz}) of the magnetic field, where FVM denotes the simulation result using Eq. (7). The simulation results of the FVM are in good agreement with those of the COMSOL. In Fig. 2, the average relative errors between the FVM results and the COMSOL results at 26, 52, and 104 kHz are 0.73%, 0.81%, and 0.72%, respectively, while those in Fig. 3 are 0.59%, 0.87%, and 0.84%. In addition, the high-conductivity mud has a large impact on the magnetic field response of the tool, and the tool eccentric distance intensifies the nonlinearity of the cross-component curve.

In the COMSOL simulations, a dense grid is used to ensure computational stability and accuracy. When the geometric position of the model changes, the mesh needs to be redivided, and the number of degrees of freedom solved by COMSOL is approximately 8.6×10^6. The number of threads used in the calculation does not exceed 10, and the computation of each magnetic dipole source takes about 4.5 min. Therefore, it takes $3 \times 4.5 = 13.5$ min to calculate a model (triaxial source).

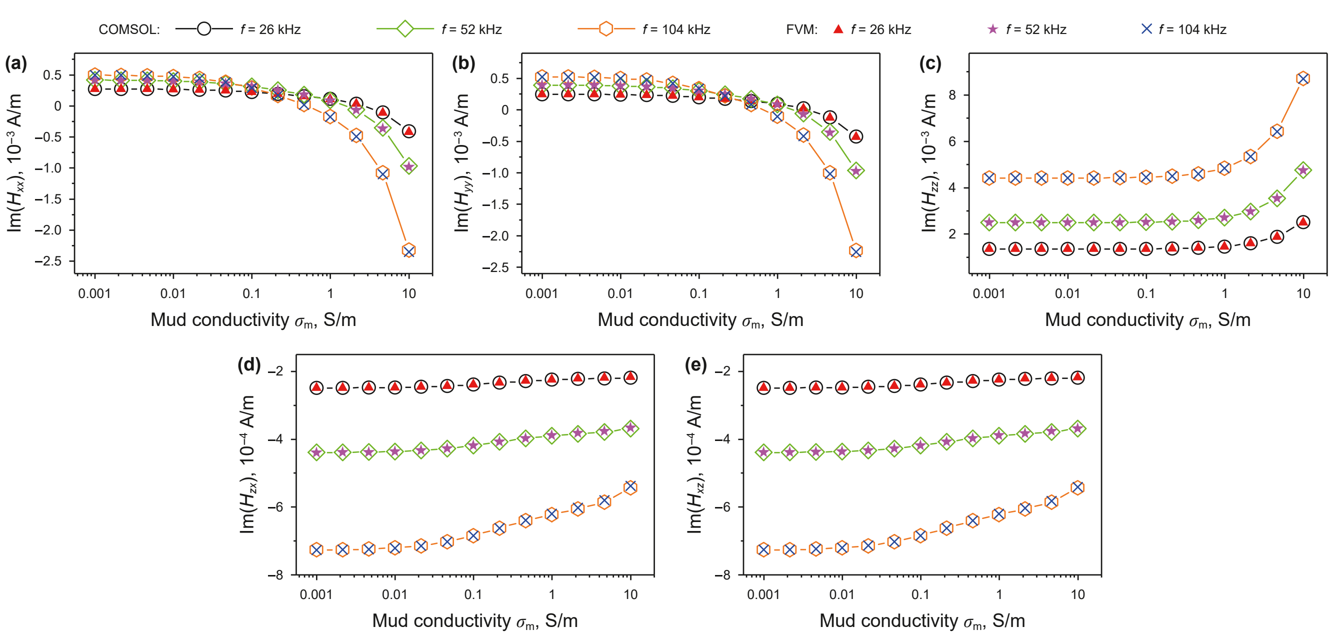

Fig. 2. Magnetic field responses under different borehole mud conductivities ($d_\mathrm{ecc} = 0$ m). **(a)**–**(c)** Three principal components H_{xx}, H_{yy}, and H_{zz}; **(d)**–**(e)** two cross components H_{zx} and H_{xz}. "Im" represents taking the imaginary part.

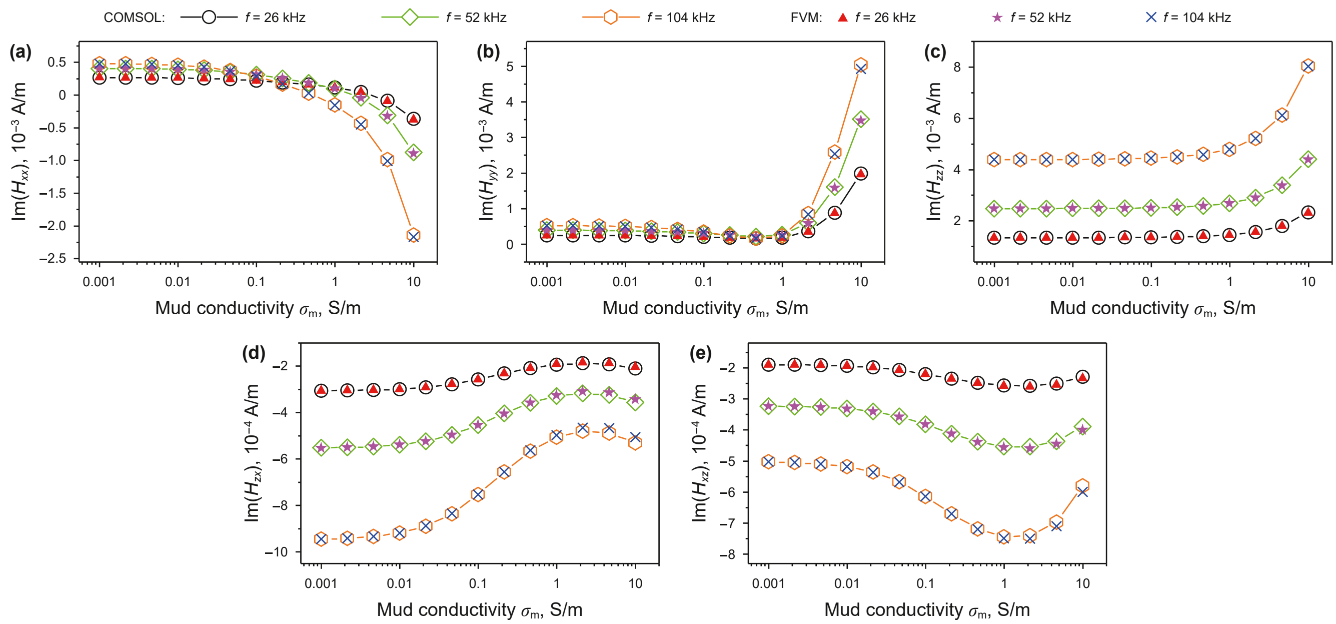

Fig. 3. Magnetic field responses under different borehole mud conductivities (d_{ecc} = 0.08 m). **(a)**–**(c)** Three principal components H_{xx}, H_{yy}, and H_{zz}; **(d)**–**(e)** two cross components H_{zx} and H_{xz}.

3.2. 3D FVM modeling efficiency

Forward modeling using Eq. (7) can simultaneously calculate the triaxial source and multiple tool eccentric distances. Suppose the formation horizontal conductivity is 0.2 S/m and the borehole mud conductivity is 1 S/m. The tool eccentric distances are chosen from Table 2, and the corresponding results are shown in Fig. 4. The effect of the tool eccentric distance on the magnetic field response is monotonic, where the *zz* component of the magnetic field is less affected by the tool eccentric distance.

The calculation results obtained from Eqs. (5) and (7) are the same. However, the matrix dimension involved in the calculation can be reduced by using Eq. (7). Although two direct solutions are required, the overall computational efficiency is still improved. Table 4 compares the time taken by PARDISO for 3D FVM modeling using Eqs. (5) and (7). Compared to using Eq. (5), Eq. (7) can increase the efficiency by a factor of 2.86. Moreover, the number of nonzero elements in the coefficient matrix $\overline{\mathbf{F}}_{xz}$ is slightly larger than that in $\overline{\mathbf{F}}_{y}$, leading to marginally longer LU factorization times for the *x*- and *z*-direction sources.

3.3. Fast calculation of different mud conductivities

The specific application of the CHBA is presented in this section. The formation horizontal conductivity is fixed at 0.2 S/m. To

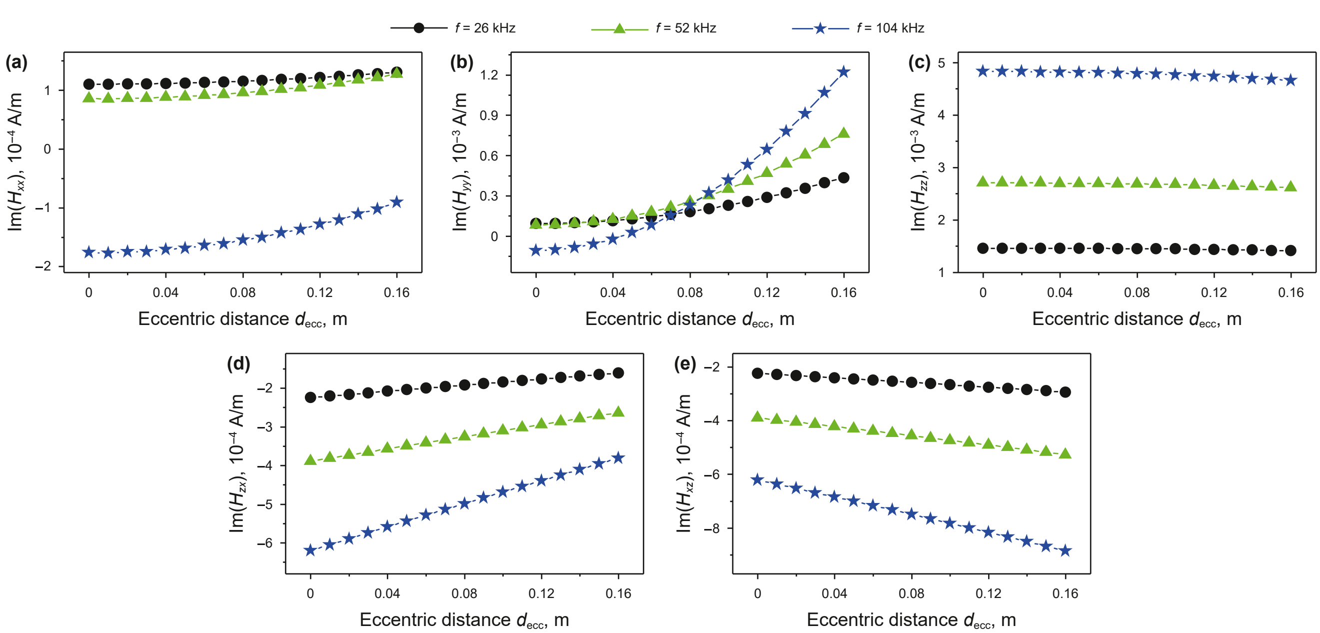

Fig. 4. Magnetic field responses under different tool eccentric distances. **(a)**–**(c)** Three principal components H_{xx}, H_{yy}, and H_{zz}; **(d)**–**(e)** two cross components H_{zx} and H_{xz}.

Table 4
Time taken by PARDISO in a 3D FVM modeling.

Equation	Source direction	Matrix dimension	Nonzero element	LU factorization		Back substitution		Total time, s
				Number	Time, s	Right-hand term	Time, s	
Eq. (5)	x, y, z	1005056	12756985	1	342.4	51	9.6	352.0
Eq. (7)	x, z	505700	6381317	1	59.9	34	2.6	123.1
	y	505700	6305885	1	58.5	17	2.1	

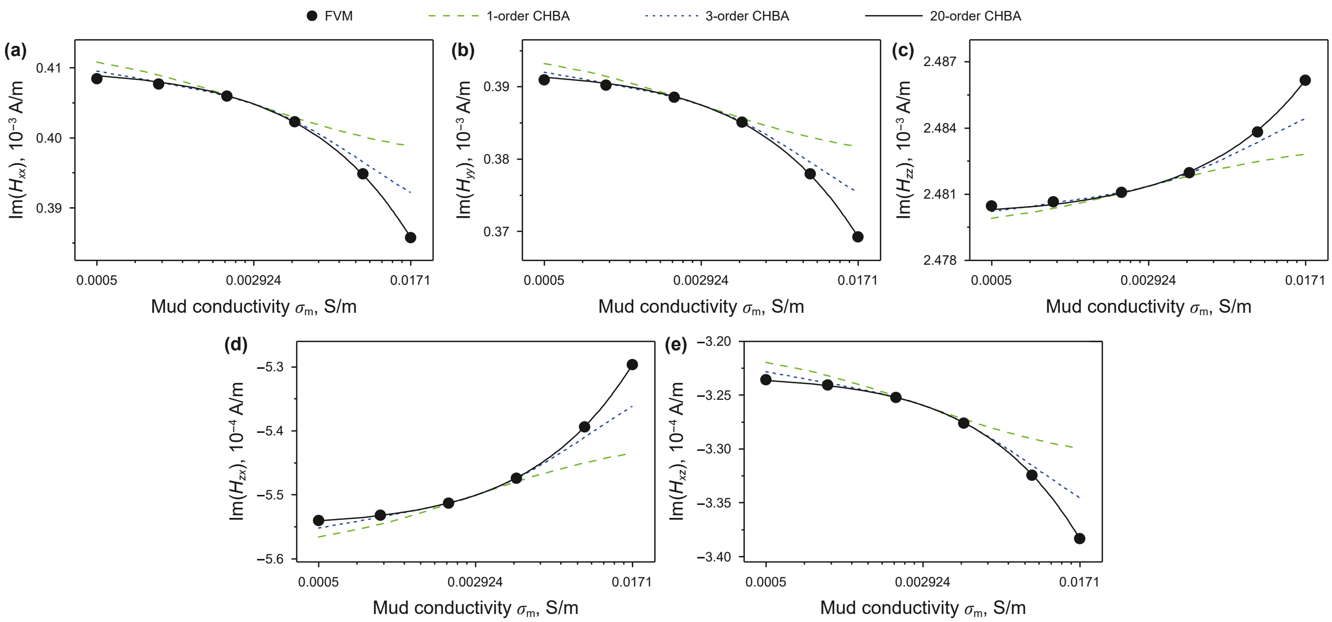

Fig. 5. The magnetic field response within the interval $\sigma_{m,\ I1}$ (f = 52 kHz). **(a)**–**(c)** Three principal components H_{xx}, H_{yy}, and H_{zz}; **(d)**–**(e)** two cross components H_{zx} and H_{xz}.

facilitate the application of the conclusions in Section 2.4, we take the frequency $f = 52$ kHz as an example and expand the range of borehole mud conductivity to [0.0005, 20] S/m. Considering the convergence rate of the CHBA, the range of the borehole mud conductivity is divided into three intervals, each solved independently using the CHBA. The specific division method is as follows: interval 1, $\sigma_{m,\ I1}$ = [0.0005, 0.0171] S/m, the reference borehole mud conductivity $\sigma_{m1} = 0.002924$ S/m; interval 2, $\sigma_{m,\ I2}$ = [0.0171, 0.5848] S/m, the reference borehole mud conductivity $\sigma_{m2} = 0.1$ S/m; interval 3, $\sigma_{m,\ I3}$ = [0.5848, 20] S/m, the reference borehole mud conductivity $\sigma_{m3} = 3.42$ S/m. The contraction factors corresponding to the borehole mud conductivities at both endpoints of the three intervals are $R = 0.708$. The truncation order of the CHBA is determined by the borehole mud conductivity at the endpoints of each interval, which ensures accuracy across the entire interval.

Based on the defined borehole mud conductivity intervals and the reference conductivity settings, the curves of the magnetic field response with the borehole mud conductivity in intervals $\sigma_{m,\ I1}$, $\sigma_{m,\ I2}$, and $\sigma_{m,\ I3}$ are given in Figs. 5–7, respectively, where the tool eccentric distance is 0.08 m. These figures compare the results obtained from the 1-order, 3-order, and 20-order CHBA with the FVM solutions, demonstrating that the more orders are used in the CHBA, the better the approximate solution obtained matches the exact solution. Based on the method proposed in our previous work (Wang et al., 2025c), the truncation order can be determined as 15. To further ensure computational stability, we set the truncation order to 20 in this study.

Table 5 presents the computational time required by PARDISO across the three borehole mud conductivity intervals. The full forward modeling of the reference model in each borehole mud conductivity interval includes the two LU factorizations and the backward substitution procedure for the 34 + 17 = 51 right-hand sides. Different model parameters do not significantly affect the efficiency of 3D FVM modeling, which averages approximately 123 s. On this basis, the 20-order CHBA requires back substitution for a total of 51 × 20 = 1020 right-hand sides and consumes roughly 94 s. By integrating the full 3D forward modeling with the CHBA, the magnetic field response across the entire borehole mud conductivity range is rapidly computed in a total time of 651.3 s. In contrast, the conventional method would necessitate 24 full forward simulations for 24 borehole mud conductivities, taking 123 × 24 = 2952 s. Therefore, employing CHBA for borehole mud conductivity can further increase the efficiency by a factor of 4.53. Moreover, another advantage of CHBA is that the sampling nodes for the mud conductivity can be very densely distributed and the additional time required can be disregarded. Finally, the memory consumption of the program during the calculation does not exceed 15 GB.

3.4. Equivalent calculations in library

In this section, we will discuss the equivalent calculations involved in the library. First, we verify the feasibility of equivalent calculations. For this purpose, the following three sets of models are set up: 1) f = 26 kHz, (σ_m, σ_h) = (0.04, 0.08), (0.08, 0.16), (0.16, 0.32), (0.32, 0.64), (0.64, 1.28), (1.28, 2.56) S/m; 2) f = 52 kHz, (σ_m, σ_h) = (0.02, 0.04), (0.04, 0.08), (0.08, 0.16), (0.16, 0.32), (0.32, 0.64), (0.64, 1.28) S/m; 3) f = 104 kHz, (σ_m, σ_h) = (0.01, 0.02), (0.02, 0.04), (0.04, 0.08), (0.08, 0.16), (0.16, 0.32), (0.32, 0.64) S/m. Fig. 8 presents the magnetic field responses in the above three sets of

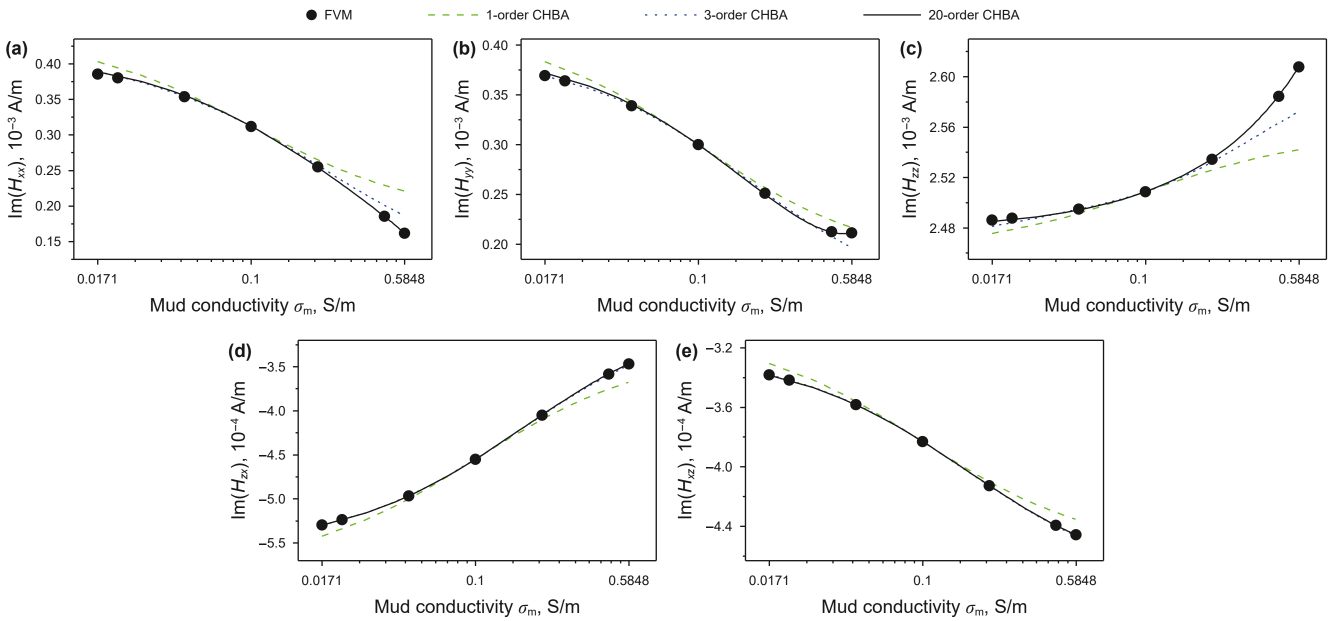

Fig. 6. The magnetic field response within the interval $\sigma_{m,\ I2}$ (f = 52 kHz). **(a)**–**(c)** Three principal components H_{xx}, H_{yy}, and H_{zz}; **(d)**–**(e)** two cross components H_{zx} and H_{xz}.

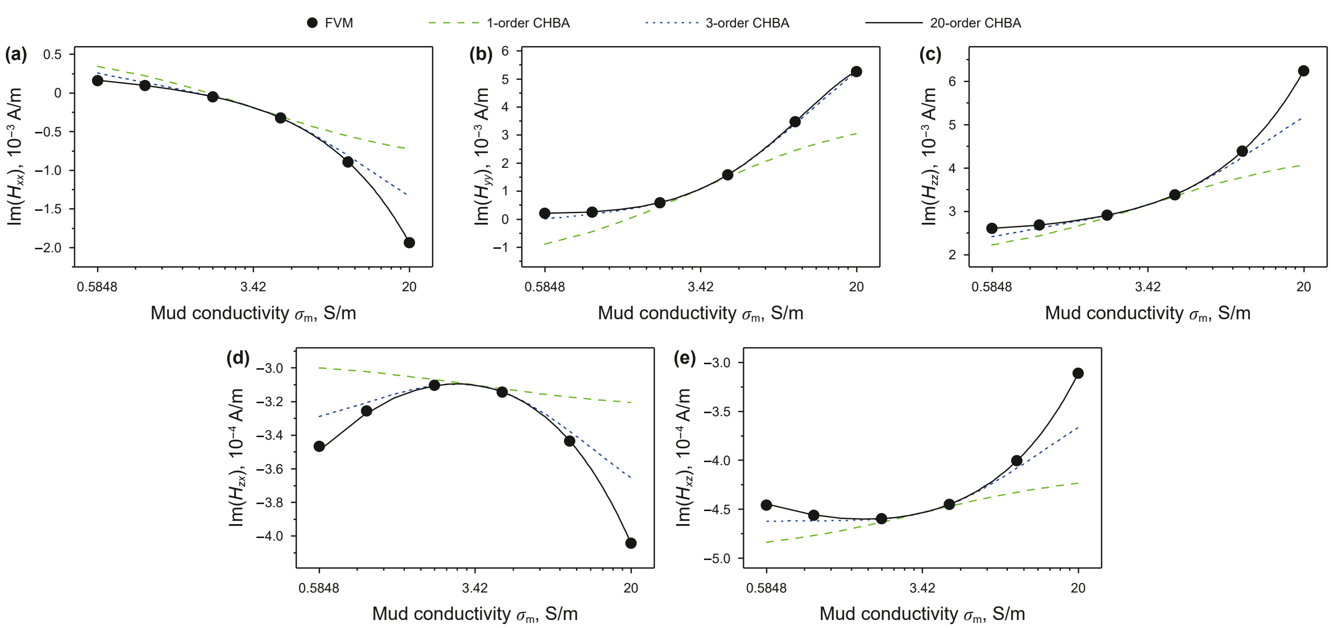

Fig. 7. The magnetic field response within the interval $\sigma_{m,\ I3}$ (f = 52 kHz). **(a)**–**(c)** Three principal components H_{xx}, H_{yy}, and H_{zz}; **(d)**–**(e)** two cross components H_{zx} and H_{xz}.

Table 5
Time taken by PARDISO in the three borehole mud conductivity intervals.

Interval	Source direction	Reference model, FVM				CHBA, $L_{\mathrm{CHBA}} = 20$		Total time, s
		LU factorization		Back substitution		Back substitution		
		Number	Time, s	Right-hand term	Time, s	Right-hand term	Time, s	
$\sigma_{m,\ I1}$	x, z	1	59.7	34	2.6	$34 \times 20 = 680$	52.5	651.3
	y	1	58.5	17	2.1	$17 \times 20 = 340$	42.4	
$\sigma_{m,\ I2}$	x, z	1	59.7	34	2.6	$34 \times 20 = 680$	51.7	
	y	1	58.4	17	2.1	$17 \times 20 = 340$	42.7	
$\sigma_{m,\ I3}$	x, z	1	59.8	34	2.5	$34 \times 20 = 680$	50.3	
	y	1	58.6	17	2.2	$17 \times 20 = 340$	42.9	

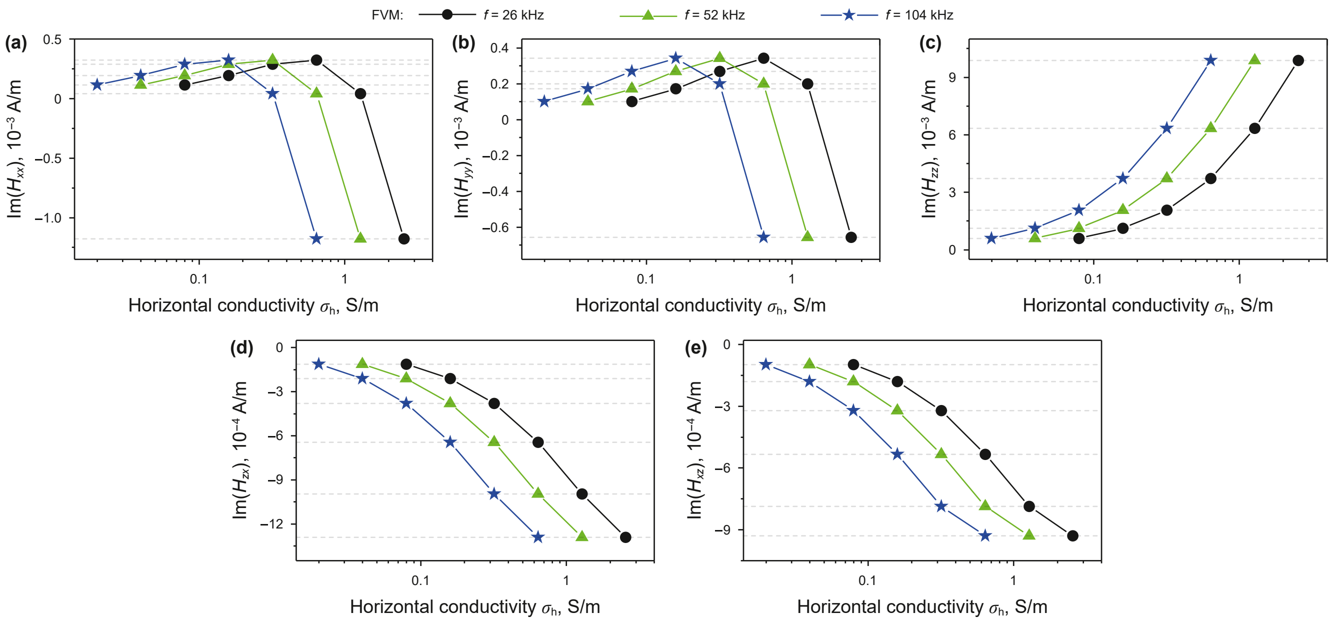

Fig. 8. Magnetic field responses corresponding to different frequencies and conductivity. **(a)–(c)** Three principal components H_{xx}, H_{yy}, and H_{zz}; **(d)–(e)** two cross components H_{zx} and H_{xz}.

models with the formation horizontal conductivity as the abscissa. It can be seen that the frequency $f = 26$ kHz and the conductivity parameter ($\sigma_{\rm m}$, $\sigma_{\rm h}$); the frequency $f = 52$ kHz, the conductivity parameter ($\sigma_{\rm m}/2$, $\sigma_{\rm h}/2$); the frequency $f = 104$ kHz, the conductivity parameter ($\sigma_{\rm m}/4$, $\sigma_{\rm h}/4$) have the same magnetic field responses. In this way, it is not necessary to calculate all the model conductivities at each frequency when building the library.

The numerical results in Section 3.3 indicate that we can quickly obtain the numerical simulation results within the entire mud conductivity range [0.0005, 20] S/m. Therefore, when considering the equivalent calculations, only the formation horizontal conductivity needs to be focused on. For practical implementations, only a total of 46 formation horizontal conductivities need to be calculated, as shown in Table 6. Through using equivalent calculations, the original $3 \times 24 = 72$ forward modeling can be reduced to 46, achieving a computational efficiency improvement by a factor of 1.56.

3.5. Construction of borehole correction library

This section outlines the construction of the borehole correction library based on the induction tool developed by China Petroleum Logging Company, Ltd. Each receiver module of the tool is composed of two triaxial receivers (the triaxial main receiver and the triaxial bucking receiver), and the magnetic field responses obtained from the two receivers are synthesized to generate the apparent conductivity response $\sigma_{{\rm a},ij}$, $i, j = x, y, z$ for each receiver module (Zhu et al., 2017). Taking the two long-spacing receiver modules in the tool as examples, the transmitter-receiver spacings of the four triaxial receivers range from 1 to 2.4 m. Fig. 9 presents an apparent conductivity chart composed of borehole mud conductivity and formation horizontal conductivity (the tool eccentric distance $d_{\rm ecc} = 0.08$ m); while Fig. 10 displays a chart composed of borehole mud conductivity and tool eccentric distance (the formation horizontal conductivity $\sigma_{\rm h} = 0.2$ S/m). Among Figs. 9 and 10, (a1–a5) and (b1–b5) correspond to two receiver modules with different spacings. As can be seen from the above figures, high-resistance mud has a relatively small effect on the tool response, while low-resistance mud has a relatively large effect. The tool is more sensitive to low-resistance formation, where the nonlinearity of the tool response is relatively strong.

Finally, we assess the computational workload required to construct the borehole correction library. Following the proposed algorithm, we consider the formation horizontal conductivity, the borehole mud conductivity, and the tool eccentric distance as the basic unit of the borehole correction library. Fig. 11 shows the efficiency improvements achieved by the three proposed strategies in the study. The conventional algorithm necessitates sequential forward modeling for 3 frequencies, 24 borehole mud conductivities, and 24 formation horizontal conductivities, requiring roughly 352.0 s $\times$ 1728 = 168.96 h. According to the algorithm efficiency given in Sections 3.2–3.4, calculating one basic unit requires 651.3 s $\times$ 46 = 8.32 h. Overall, the proposed algorithm achieves a 20-fold improvement in efficiency. For the model parameters listed in Table 2, the library comprises $15 \times 9 \times 15 = 2025$ basic units, projecting a total computational duration of 16848 h (approximately 702 days). Therefore, to complete the borehole correction library within a feasible timeframe, it is necessary to minimize the number of parameter nodes as much as possible and use more computational resources.

Table 6
Formation horizontal conductivity nodes for three frequencies.

Frequency	Number of nodes	Nodes
52 kHz	24	0.001, 0.01, 0.02, 0.04, 0.08, 0.1, 0.2, 0.3, 0.4, 0.5, 0.6, 0.7, 0.8, 0.9, 1, 2, 3, 4, 5, 6, 7, 8, 9, 10 S/m
26 kHz	11	0.001, 0.01, 0.1, 0.3, 0.5, 0.7, 0.9, 3, 5, 7, 9 S/m
104 kHz	11	0.001, 0.08, 0.6, 0.7, 0.8, 0.9, 6, 7, 8, 9, 10 S/m

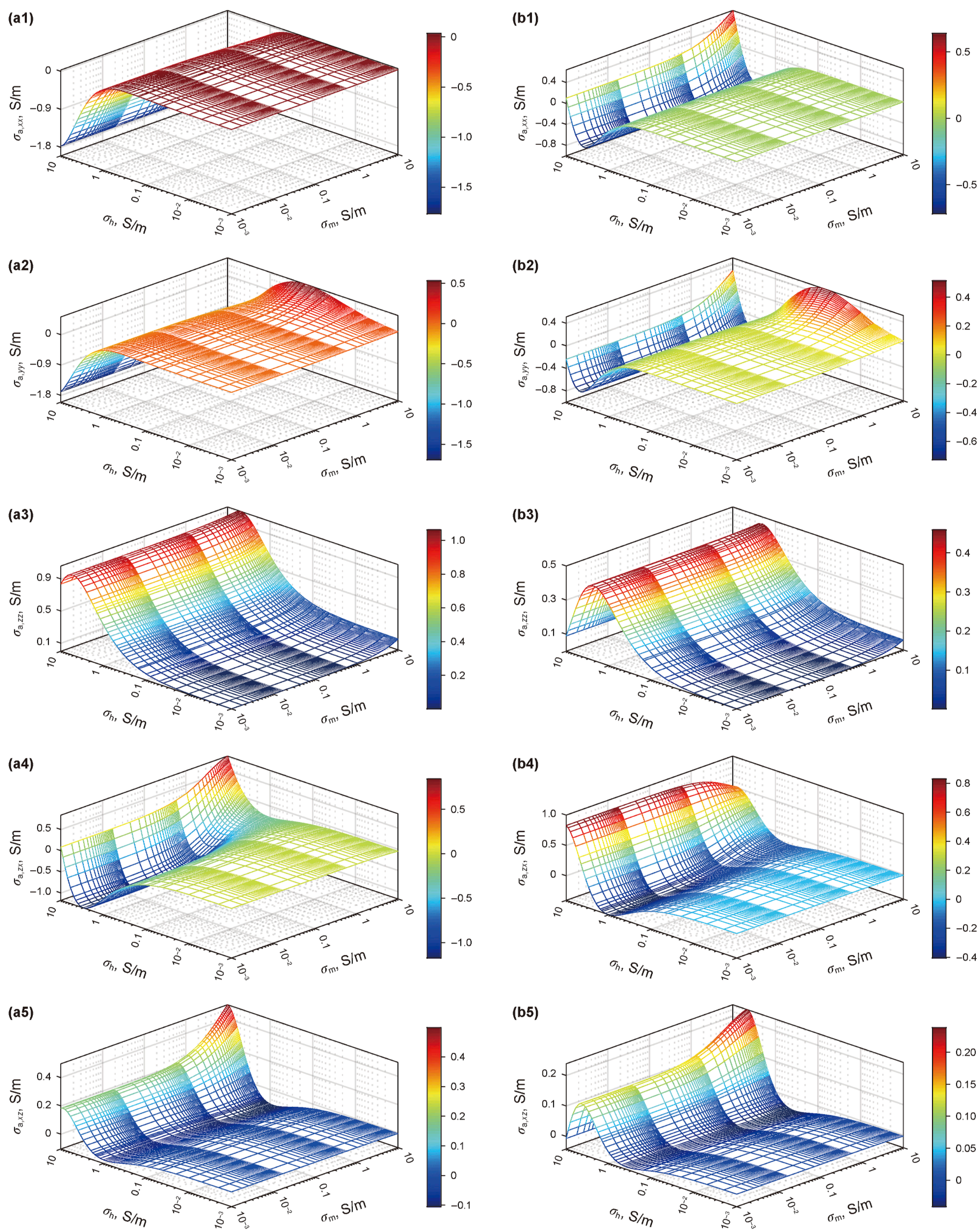

Fig. 9. Apparent conductivity chart composed of borehole mud conductivity and formation horizontal conductivity (d_{ecc} = 0.08 m). **(a1)–(a5)** and **(b1)–(b5)** correspond to two receiver modules with different spacings.

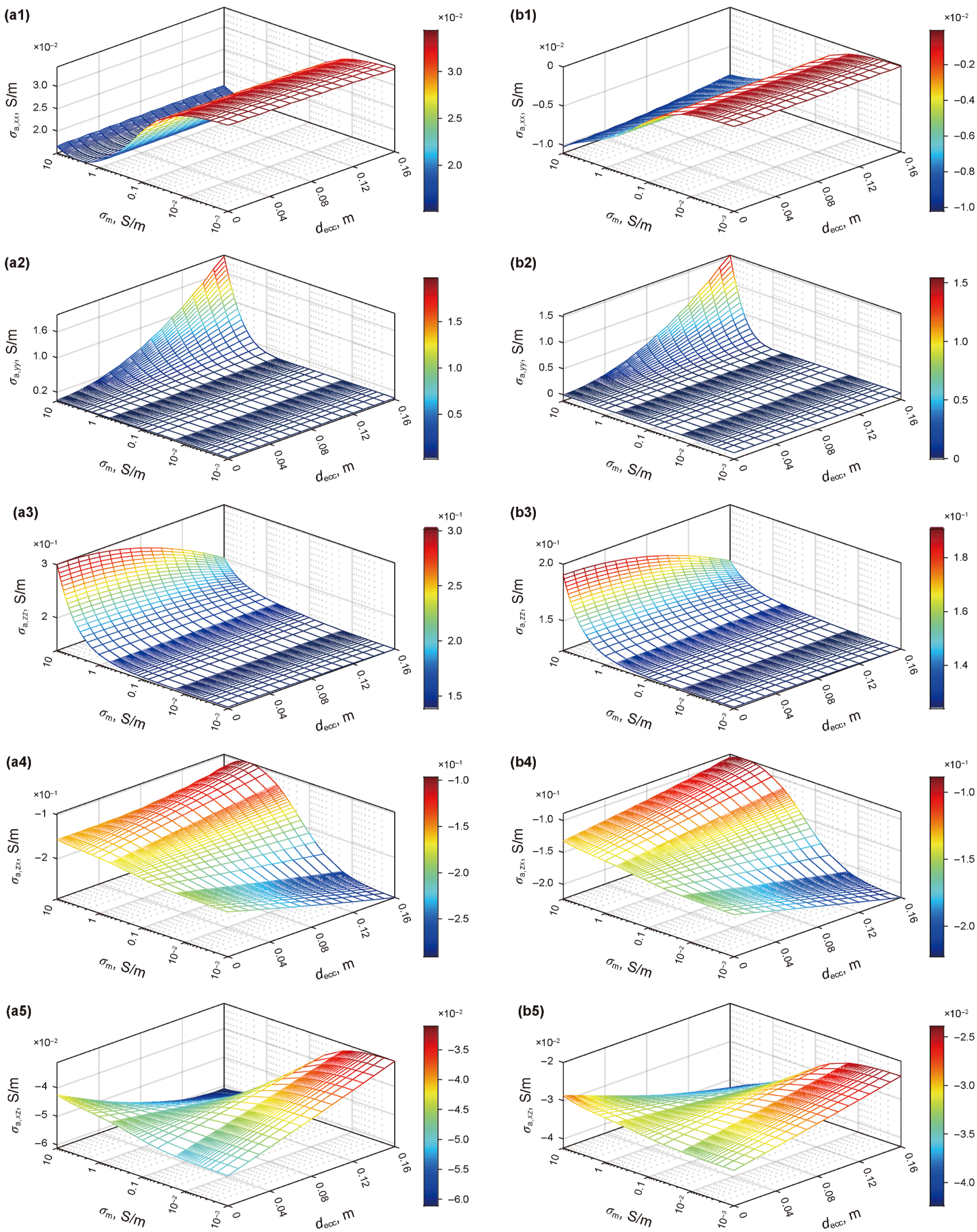

Fig. 10. Apparent conductivity chart composed of borehole mud conductivity and tool eccentric distance (σ_h = 0.2 S/m). **(a1)–(a5)** and **(b1)–(b5)** correspond to two receiver modules with different spacings.

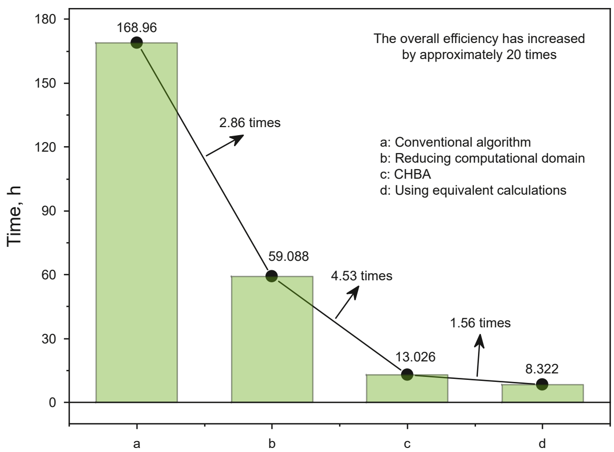

Fig. 11. The time taken to build the borehole correction library and the efficiency improvement of the different methods.

4. Conclusions

In this paper, we propose a fast method of building the borehole correction library for the multi-component array induction tool in deviated boreholes. First, the symmetry in the construction of the borehole correction library is exploited to reduce the computational workload. The triaxial source and multiple tool eccentric distances are then solved simultaneously by a direct solver. Based on the full forward modeling framework, the CHBA is applied to the borehole mud conductivity to quickly obtain the simulation results in the target mud conductivity range. Finally, the efficiency is further improved by using the equivalent calculations in the borehole correction library.

The numerical results validate the correctness and feasibility of the proposed algorithm. In terms of efficiency improvements, exploiting symmetry enhances the efficiency of 3D FVM modeling by a factor of 2.86, applying the CHBA further increases the library construction efficiency by a factor of 4.53, while using the equivalent calculations yields an additional 1.56-fold improvement. Collectively, these methods achieve approximately a 20-fold efficiency gain in building the borehole correction library.

It should be emphasized that incorporating more complex eccentricity conditions (asymmetric models) not only necessitates more eccentricity nodes but also increases the time required for each forward modeling. This remains a challenging problem. Furthermore, the operating frequencies of the considered tool differ by a factor of two. If the frequency multiples employed by the tool are not equal, the difficulty of matching conductivity nodes with frequencies during the equivalent calculation will also increase. Finally, even though the proposed algorithm can significantly improve the efficiency, building a complete library remains computationally intensive. It is necessary to consider further enhancing algorithmic efficiency (e.g., implementing the octree method to reduce the grid number), minimizing the number of model parameter nodes as much as possible, and utilizing more computational resources.

CRediT authorship contribution statement

Ya-Zhou Wang: Writing – original draft. **Hong-Nian Wang:** Writing – review & editing. **Lei Yu:** Writing – review & editing. **Yan Bai:** Resources. **Shou-Wen Yang:** Resources.

Declaration of competing interests

The authors declare that they have no known competing financial interests or personal relationships that could have appeared to influence the work reported in this paper.

Acknowledgements

This research has been funded by the Forward-looking Basic Science and Technology Research Project of PetroChina Company Limited (2025DJ104), the National Natural Science Foundation of China (42174150) and the National Science and Technology Major Project for Deep Earth Probe and Mineral Resources Exploration (2024ZD1003005).

Appendix

The expansion of the change in the electric field given in the CHBA is

$$\Delta\mathbf{E}(\mathbf{r},\mathbf{r}_\mathrm{T}) = \frac{2\sqrt{\overline{\boldsymbol{\sigma}}(\mathbf{r})}\cdot\boldsymbol{\chi}(\mathbf{r},\mathbf{r}_\mathrm{T}) - \mathbf{J}(\mathbf{r},\mathbf{r}_\mathrm{T})}{2\overline{\boldsymbol{\sigma}}(\mathbf{r}) + \Delta\overline{\boldsymbol{\sigma}}_k(\mathbf{r})}, \tag{A1}$$

where $\boldsymbol{\chi}(\mathbf{r},\mathbf{r}_\mathrm{T})$ is

$$\boldsymbol{\chi}(\mathbf{r},\mathbf{r}_\mathrm{T}) = \sum_{l=1}^{\infty}\boldsymbol{\chi}_l(\mathbf{r},\mathbf{r}_\mathrm{T}),$$

$$\boldsymbol{\chi}_l(\mathbf{r},\mathbf{r}_\mathrm{T}) = \begin{cases} \sqrt{\overline{\boldsymbol{\sigma}}(\mathbf{r})}\cdot\boldsymbol{\lambda}_l(\mathbf{r},\mathbf{r}_\mathrm{T}) + \dfrac{\sqrt{\overline{\boldsymbol{\sigma}}(\mathbf{r})}}{2\overline{\boldsymbol{\sigma}}(\mathbf{r}) + \Delta\overline{\boldsymbol{\sigma}}(\mathbf{r})}\cdot\mathbf{J}(\mathbf{r},\mathbf{r}_\mathrm{T}), l=1 \\ \sqrt{\overline{\boldsymbol{\sigma}}(\mathbf{r})}\cdot\boldsymbol{\lambda}_l(\mathbf{r},\mathbf{r}_\mathrm{T}) + \overline{\mathbf{R}}(\mathbf{r})\cdot\boldsymbol{\chi}_{l-1}(\mathbf{r},\mathbf{r}_\mathrm{T}), l=2,3,\cdots \end{cases}, \tag{A2}$$

and here, $\Delta\overline{\boldsymbol{\sigma}}(\mathbf{r})$ is the tensor of change in conductivity, $\overline{\mathbf{R}}(\mathbf{r}) = \frac{\Delta\overline{\boldsymbol{\sigma}}(\mathbf{r})}{2\overline{\boldsymbol{\sigma}}(\mathbf{r})+\Delta\overline{\boldsymbol{\sigma}}(\mathbf{r})}$ is the tensor contraction factor, and the scattered electric field $\boldsymbol{\lambda}_l(\mathbf{r},\mathbf{r}_\mathrm{T})$ satisfies Eq. (11).

By using

$$[1-\overline{\mathbf{R}}(\mathbf{r})]^{-1} = \frac{2\overline{\boldsymbol{\sigma}}(\mathbf{r}) + \Delta\overline{\boldsymbol{\sigma}}_k(\mathbf{r})}{2\overline{\boldsymbol{\sigma}}(\mathbf{r})} = \sum_{l=1}^{\infty}\overline{\mathbf{R}}(\mathbf{r})^l, \tag{A3}$$

the Eq. (A2) can be further simplified to

$$\begin{aligned} \boldsymbol{\chi}(\mathbf{r},\mathbf{r}_\mathrm{T}) &= \sum_{l=1}^{\infty}\boldsymbol{\chi}_l(\mathbf{r},\mathbf{r}_\mathrm{T}) \\ &= \frac{\sqrt{\overline{\boldsymbol{\sigma}}(\mathbf{r})}}{2\overline{\boldsymbol{\sigma}}(\mathbf{r}) + \Delta\overline{\boldsymbol{\sigma}}(\mathbf{r})}\cdot\sum_{l=0}^{\infty}\overline{\mathbf{R}}(\mathbf{r})^l\cdot\mathbf{J}(\mathbf{r},\mathbf{r}_\mathrm{T}) + \sqrt{\overline{\boldsymbol{\sigma}}(\mathbf{r})}\cdot\sum_{l=0}^{\infty}\overline{\mathbf{R}}(\mathbf{r})^l\cdot\sum_{l=1}^{\infty}\boldsymbol{\lambda}_l(\mathbf{r},\mathbf{r}_\mathrm{T}) \\ &= \frac{\sqrt{\overline{\boldsymbol{\sigma}}(\mathbf{r})}}{2\overline{\boldsymbol{\sigma}}(\mathbf{r})}\cdot\mathbf{J}(\mathbf{r},\mathbf{r}_\mathrm{T}) + \frac{2\overline{\boldsymbol{\sigma}}(\mathbf{r}) + \Delta\overline{\boldsymbol{\sigma}}(\mathbf{r})}{2\sqrt{\overline{\boldsymbol{\sigma}}(\mathbf{r})}}\cdot\sum_{l=1}^{\infty}\boldsymbol{\lambda}_l(\mathbf{r},\mathbf{r}_\mathrm{T}). \end{aligned} \tag{A4}$$

Substituting Eq. (A4) into Eq. (A1) eventually resulted in the simplified expansion Eq. (10).

References

Avdeev, D.B., Kuvshinov, A.V., Pankratov, O.V., et al., 2002. Three-dimensional induction logging problems, Part I: An integral equation solution and model comparisons. Geophysics 81 (1), 413–426. https://doi.org/10.1190/1.1468601.

Bai, Y., Yang, S.W., Ma, Y.G., et al., 2018. Adaptive borehole correction of three-dimensional array induction logging data in a vertical borehole. Chin. J. Geophys. 61 (9), 3876–3888 (in Chinese). https://doi.org/10.6038/cjg2018L0082.

Chen, G.B., Zhang, Y., Lu, J., 2021. Contraction integral equation for modeling of EM scattering by 3-D bodies buried in multilayered anisotropic medium. IEEE Trans. Antenn. Propag. 69 (2), 962–970. https://doi.org/10.1109/TAP.2020.3026903.

Davydycheva, S., Homan, D., Minerbo, G., 2009. Triaxial induction tool with electrode sleeve FD modeling in 3D geometries. J. Appl. Geophys. 67 (1), 98–108. https://doi.org/10.1016/j.jappgeo.2008.10.001.
Deng, S.G., Liu, T.L., Cai, L.Y., et al., 2021. Fast extraction of horizontal formation resistivity based on multi-component induction logging and its application. Chin. J. Geophys. 64 (6), 2199–2209 (in Chinese). https://doi.org/10.6038/cjg2021O0265.
Haber, E., Ascher, U.M., Aruliah, D.A., et al., 2000. Fast simulation of 3D electromagnetic problems using potentials. J. Comput. Phys. 163 (1), 150–171. https://doi.org/10.1006/jcph.2000.6545.
Hou, J.S., Bittar, M., 2010. Correction for the borehole effect of multi-component array induction log data. In: Electromagnetics Research Symposium Proceedings, pp. 403–409.
Hou, J.S., Sanmartin, L., Wu, D.G., et al., 2013a. A new multi-frequency triaxial array induction tool for enhancing evaluation of anisotropic formations and its field testing. In: SPWLA 54th Annual Logging Symposium.
Hou, J.S., Sanmartin, L., Wu, D.G., et al., 2013b. Real-time borehole correction of multicomponent induction data acquired in OBM wells algorithm and applications. Petrophysics 54 (2), 128–141.
Hussain, F., Mubark, S., Aldred, R., et al., 2005. Contributions of multi-component induction logs in difficult wellbore environments in North Kuwait low resistivity pay evaluation. In: SPWLA 46th Annual Logging Symposium.
Li, F.B., Wu, Z.G., Ni, W.N., et al., 2025. A simplified 3D finite difference method for electromagnetic logging while drilling simulation in symmetrical models. Front. Earth Sci. 13, 1539368. https://doi.org/10.3389/feart.2025.1539368.
Saputera, D.H., Jakobsen, M., Dongen, K.W.A., et al., 2024. 3-D induction log modelling with integral equation method and domain decomposition pre-conditioning. Geophys. J. Int. 236 (2), 834–848. https://doi.org/10.1093/gji/ggad454.
Sun, Q.T., Hu, Y.Y., 2022. Fast geometric multigrid preconditioned finite-difference frequency-domain method for borehole electromagnetic sensing. IEEE Geosci. Rem. Sens. Lett. 19, 8007404. https://doi.org/10.1109/LGRS.2021.3053590.
Wang, C.X., Chu, Z.T., Xiao, C.W., et al., 2013. The analysis of effect of the borehole environment on responses of array induction logging. Chin. J. Geophys. 56 (4), 1392–1403 (in Chinese). https://doi.org/10.6038/cjg20130433.
Wang, H.N., Wang, Y.Z., Yu, L., et al., 2024a. 3-D adaptive regularization nonlinear inversion of LWD ultradeep resistivity in anisotropic formation based on finite volume method of secondary field coupled potentials and explicit Fréchet derivative. IEEE Trans. Geosci. Rem. Sens. 62, 5919614. https://doi.org/10.1109/TGRS.2024.3421568.
Wang, H.S., Yang, S.W., Wang, H.N., 2024b. Efficient simulation of LWD azimuthal propagation resistivity tool in layered TI formation based on 3-D finite volume method of coupled potentials in the half space and continuation technique. IEEE Access 12, 190912–190921.
Wang, L., Cao, F.H., Li, Z.Q., et al., 2024c. A novel propagator coefficient algorithm for modeling induction-type logging responses in cylindrically layered media. IEEE Geosci. Rem. Sens. Lett. 21, 7504505. https://doi.org/10.1109/LGRS.2024.3401126.
Wang, L., Han, Y.Y., Li, Z.Q., et al., 2025a. The joint physics and data-driven geometrical factor of array laterolog in layered formations. Geophysics 90 (1), D11–D25. https://doi.org/10.1190/GEO2024-0112.1.
Wang, L., Liu, Y.M., Wang, C.Z., et al., 2021. Real-time forward modeling and inversion of logging-while-drilling electromagnetic measurements in horizontal wells. Petrol. Explor. Dev. 48 (1), 159–168. https://doi.org/10.1016/S1876-3804(21)60012-5.
Wang, L., Qiao, P., Li, Z.Q., et al., 2023a. A new semianalytical algorithm for rapid simulation of triaxial electromagnetic logging responses in multilayered biaxial anisotropic formations. Geophysics 88 (2), D115–D129. https://doi.org/10.1190/geo2021-0714.1.
Wang, Y.Z., Wang, H.N., Kang, Z.Z., et al., 2023b. Efficient computation of nonlinear born approximation of the LWD ultra-deep look ahead resistivity measurement using coupled potentials 3D finite-volume method and differential operator expansion. Chin. J. Geophys. 66 (7), 3102–3114 (in Chinese). https://doi.org/10.6038/cjg2022Q0650.
Wang, Y.Z., Wang, H.N., Yang, S.W., et al., 2025b. Fast 3-D modeling of the LWD ultradeep resistivity measurements using the field-based secondary-field finite volume method. IEEE Trans. Geosci. Rem. Sens. 63, 5906216. https://doi.org/10.1109/TGRS.2025.3536792.
Wang, Y.Z., Wang, H.N., Yu, L., et al., 2025c. Efficient algorithm of contraction high-order born approximation on LWD ultra-deep resistivity measurement in 3-D anisotropic formation. IEEE Trans. Geosci. Rem. Sens. 63, 5900112. https://doi.org/10.1109/TGRS.2024.3511666.
Wu, Y.Z., Wu, Z.G., Fan, Y.R., et al., 2022. Numerical and physical simulations of array laterolog in deviated anisotropic formation. Pet. Sci. 19 (5), 2107–2119. https://doi.org/10.1016/j.petsci.2022.03.023.
Wu, Z.G., Deng, S.G., He, X.Q., et al., 2020. Numerical simulation and dimension reduction analysis of electromagnetic logging while drilling of horizontal wells in complex structures. Pet. Sci. 17, 645–657. https://doi.org/10.1007/s12182-020-00444-y.
Wu, Z.G., Li, H., Yue, X.Z., 2023. 2.5-Dimensional modeling of EM logging-while-drilling tool in anisotropic medium on a Lebedev grid. Pet. Sci. 20 (1), 249–260. https://doi.org/10.1016/j.petsci.2022.09.010.
Yan, L., Zeng, S.B., Chen, J.F., 2022. 2-D pixel-based inversion for simultaneous reconstruction of resistivity and dielectric constant from electromagnetic logging-while-drilling measurements. IEEE Trans. Geosci. Rem. Sens. 60, 2002114. https://doi.org/10.1109/TGRS.2021.3092599.
Yu, L., Wang, H.N., Wang, H.S., et al., 2022. 3-D finite volume modeling for LWD azimuthal propagation resistivity tool with multiple annular antenna recesses using coupled potentials on cylindrical grids. IEEE Trans. Antenn. Propag. 70 (1), 514–525. https://doi.org/10.1109/TAP.2021.3098522.
Yu, L., Wang, H.N., Wang, Y.Z., et al., 2024. Adaptive global optimization of real-time boundary detection from the LWD azimuthal electromagnetic measurements in layered TI formation with arbitrarily deviated borehole. IEEE Trans. Geosci. Rem. Sens. 62, 5903115. https://doi.org/10.1109/TGRS.2024.3352901.
Yuan, C., Li, C.L., Zhou, C.C., et al., 2020. Forward simulation of array laterolog resistivity in anisotropic formation and its application. Petrol. Explor. Dev. 47 (1), 80–88 (in Chinese). https://doi.org/10.1016/S1876-3804(20)60007-6.
Zhao, J., Pei, H.C., Luo, L., 2025. Anisotropic response characteristics of array induction logging in laminated shale and its correction methods. SPE J. 30 (2), 729–742. https://doi.org/10.2118/223961-PA.
Zhu, T.Z., Yang, S.W., Bai, Y., et al., 2017. Efficient and high-precision establishment of borehole correction database for multicomponent array induction logging in vertical boreholes by a 2.5D NMM algorithm. Chin. J. Geophys. 60 (3), 1221–1233 (in Chinese). https://doi.org/10.6038/cjg20170332.